PAPER

Inkjet 3D printing of UV and thermal cure silicone elastomers for dielectric elastomer actuators

IOP Publishing Smart Materials and Structures
Smart Mater. Struct. **26** (2017) 125022 (17pp) https://doi.org/10.1088/1361-665X/aa9695

Inkjet 3D printing of UV and thermal cure silicone elastomers for dielectric elastomer actuators

David McCoul, Samuel Rosset[1], Samuel Schlatter and Herbert Shea

École Polytechnique Fédérale de Lausanne (EPFL), Microsystems for Space Technologies Laboratory (LMTS), CH-2000 Neuchâtel, Switzerland

E-mail: herbert.shea@epfl.ch

Received 1 September 2017, revised 17 October 2017
Accepted for publication 27 October 2017
Published 10 November 2017

Abstract

Dielectric elastomer actuators (DEAs) are an attractive form of electromechanical transducer, possessing high energy densities, an efficient design, mechanical compliance, high speed, and noiseless operation. They have been incorporated into a wide variety of devices, such as microfluidic systems, cell bioreactors, tunable optics, haptic displays, and actuators for soft robotics. Fabrication of DEA devices is complex, and the majority are inefficiently made by hand. 3D printing offers an automated and flexible manufacturing alternative that can fabricate complex, multi-material, integrated devices consistently and in high resolution. We present a novel additive manufacturing approach to DEA devices in which five commercially available, thermal and UV-cure DEA silicone rubber materials have been 3D printed with a drop-on-demand, piezoelectric inkjet system. Using this process, 3D structures and high-quality silicone dielectric elastomer membranes as thin as 2 μm have been printed that exhibit mechanical and actuation performance at least as good as conventionally blade-cast membranes. Printed silicone membranes exhibited maximum tensile strains of up to 727%, and DEAs with printed silicone dielectrics were actuated up to 6.1% area strain at a breakdown strength of 84 V μm^{-1} and also up to 130 V μm^{-1} at 2.4% strain. This approach holds great potential to manufacture reliable, high-performance DEA devices with high throughput.

Keywords: 3D printing, silicone, inkjet, drop-on-demand, dielectric elastomer actuator

(Some figures may appear in colour only in the online journal)

1. Introduction and motivation

Dielectric elastomer actuators (DEAs) have garnered much interest as a novel form of electromechanical transducer as they possess high energy densities, an efficient design able to perform work with a minimum of components, mechanical compliance, high speed, and noiseless operation [1–4]. Their structure consists of an elastomeric dielectric layer such as silicone rubber sandwiched between two flexible, overlapping electrodes, often containing carbon as the conducting material [5–7]. When these electrodes are charged with a high voltage in much the same way a parallel plate capacitor is charged, the resulting electric field creates a Maxwell pressure that deforms the elastomer, increasing its planar area and decreasing its thickness. DEAs have been incorporated into a variety of elegant devices, such as active microfluidic channels [8–10], cell bioreactors [11, 12], tunable optics [13] and RF phase-shifters [14], refreshable haptic displays [15, 16], medical robotics [17–22], and soft robots that can grasp [23–26], walk, crawl, hop, and fly [27, 28].

In this paper, we present a novel approach to manufacturing DEA-based devices by utilizing drop-on-demand (DOD) inkjet 3D printing to build dielectric membranes from standard silicone elastomer materials. Silicone membranes and multilayer structures were 3D-printed with layer thicknesses as low as 2 μm. Both two-part thermal cure and a

[1] Now with Biomimetics Lab, Auckland Bioengineering Institute, The University of Auckland, Auckland, New Zealand.

single-part UV cure silicones were shown to be compatible with this process. The printed thermal-cure and UV-cure silicone elastomers exhibited mechanical properties and DEA performance at least as good as those of their blade-cast counterparts. The work presented in this paper is the first report of inkjet printing commercially available silicone elastomers for dielectric elastomers. Several challenges still remain, such as controlling nozzle clogging, as well as printing large devices in a short amount of time. However, with further refinements of the inkjet materials and print systems, one can envision this additive manufacturing approach capable of producing highly reliable DEA devices in high throughput.

More than 20 years after the pioneering work of Pelrine *et al* [29], the majority of DEA-based devices are still fabricated manually [5]. Not only is manual production potentially time-consuming and tedious, but it can also produce inconsistent results, and the production yield is difficult to optimize. As a step towards industrialization of DEA devices, efforts have been made to automate the fabrication of DEAs [19, 30, 31]. These automated fabrication machines are often large and complicated, combining many different processes such as casting, spin coating, spraying, stretching, laminating, and cutting. These machines are typically highly specialized, able to fabricate only one type of design, or part of one design, for instance a single DEA stack actuator. In this vein, none of these methods are capable of patterning the dielectric layer, limiting the design freedom of DEAs.

Bottom-up approaches involving additive manufacturing techniques such as 3D printing hold promise to overcome many of the above limitations in the fabrication of DEA-based devices. 3D printing offers many key advantages over other manufacturing methods due primarily to the aspect of computer control, which enables: (1) full automation, (2) high resolution and precision, (3) consistent results, (4) design flexibility, and (5) predictable production yields. From these advantages, devices can be produced with unique features that are: (1) highly complex if required, (2) fully integrated with no further assembly needed, (3) made from multiple independent materials, and (4) fully defined from a computer-aided design (CAD) file. Moreover, certain 3D printing techniques allow very thin ($<3\ \mu$m) layers to be printed, resulting in potentially lower DEA driving voltages. For these reasons, high-performance, 3D-printed DEA devices can be envisioned that to date have not been possible to produce.

As its name implies, additive manufacturing, the most common of which is 3D printing, involves the layer-by-layer addition of material to build three-dimensional, solid objects [32–35]. This is in contrast with more traditional approaches that remove material to shape a part, such as machining or etching. Several different types of 3D printing are commercially available. One of the most widespread is called fused deposition modeling (FDM), in which a filament of a thermoplastic such as poly(lactic acid) or acrylonitrile butadiene styrene is heated above its glass transition temperature and extruded onto a movable stage to build a three-dimensional part [36]. Traditional FDM parts are limited to the resolution of the filament diameter [37, 38]. In another approach called binder jetting (BJ), plastic and rubber-like materials can be formed from printing a binder into a powder [39, 40]. Higher resolutions can be achieved through stereolithography, whereby liquid resins of photoactive polymer precursors are locally polymerized by a focused laser beam [41, 42]. However, printing multiple materials is difficult. Metal parts can also be printed via a similar process known as direct metal laser sintering, where a metal powder is melted together through local heating by a laser [43–46]. Finally, similar to BJ, inkjet printing can build plastic and rubber-like materials by depositing drops of polymer-based ink solutions [47]. As a result, this type of inkjet printing is sometimes referred to as PolyJet printing [48]. The inks are often photoactive and can be cured layer-by-layer with an ultraviolet (UV) or infrared (IR) lamp. The high resolution, relatively low cost, and multiple material compatibility make this final 3D printing category an attractive option for 3D printing DEA-based devices. Therefore, inkjet printing is the focus of the research presented in this paper.

Additive manufacturing in the dielectric elastomer field is still in its infancy, although several basic studies have been performed in this direction. One of the simplest DEA additive manufacturing approaches utilizes aerosol spray deposition to build silicone membranes. While it is not inkjet printing, it is a deposition technique that involves the formation of droplets, and it can therefore utilize similar materials. Araromi *et al* devised a semi-automated process to spray deposit multilayered DEAs using a spray brush at 29 psi and a wheel substrate rotating at 0.68 Hz [49]. They diluted Dow Corning® Silastic® 3481 in five parts dichloromethane and filtered the solution prior to aerosol spraying. Using 5% of a 81-VF curing agent, a four-layer stack actuator was fabricated and achieved a 3.4% linear strain at a maximum 4.5 kV ($\sim$80 V μm^{-1}).

In a related effort, Reitelshöfer *et al* aerosol jet printed silicone layers and electrodes, using Wacker Elastosil® P7670 as the dielectric [50, 51]. Unlike aerosol spray deposition, aerosol jetting has a focused beam and therefore delivers an intrinsic line resolution without requiring a mask. Rather than diluting the silicone before spraying, parts A and B were mixed and then heated during aerosol jetting to lower the viscosity to a suitable level. However, the fabrication of multilayer stack DEAs using this aerosol jetting method is still under investigation. One potential advantage of our inkjet approach is that features (such as electrodes or other silicone layers) can be printed directly atop suspended membranes without deforming the membrane. For thicker devices (e.g., stacks) or devices on a rigid substrate, the deformation is less of an issue. Poulin *et al* took a different approach, utilizing pad printing to produce very thin (approximately 2 μm thick) silicone membranes and $\sim$1.5 μm thick electrodes [52]. Pad printing utilizes a PDMS stamp to automatically pick up a thin layer of material from a shallow reservoir known as a cliché and then deposit it onto a substrate. Dow Corning® Sylgard® 184 was pad printed and cured to create a membrane, which was then pad printed with one electrode and prestrained equibiaxially by 10%. The result was a 1.5 μm thick membrane with a 1–2 μm thick electrode, forming half of a DEA. Two halves were brought together and actuated, achieving a 7.5% diameter strain at 245 V (81.7 V μm^{-1}).

Some preliminary studies have been performed to inkjet 3D print DEAs. Rossiter *et al* used an inkjet Eden 350 V 3D printer (Objet Geometries, Rehorot, Israel) to attempt to print a DEA dielectric utilizing the TangoPlus FLX930 UV-curable acrylic pseudo-rubber designed for the printer by the manufacturer [53]. Three 29 μm layers of this material were printed, and the resulting 87 μm acrylate was coated with silver grease electrodes. Without prestretch, the DEA merely underwent buckling up to a breakdown strength of $\sim$60 V μm^{-1}. An antagonistic actuator with a central post was also 3D-printed, electrodes were manually applied, and at 3.6 kV it exhibited a displacement of 0.15 mm in each direction and a maximum blocking force of 0.3 N. This effort could produce high-resolution structures down to 42 μm in the planar dimensions and 29 μm in the z-direction. However, the printed pseudo-rubber material lacks the standard mechanical and electrical integrity of commercially available DEA elastomers. Simply put, standard materials that can be printed with commercial 3D printers are not suitable for DEA dielectrics or electrodes.

In addition to printing the dielectric material, electrodes have also been inkjet printed in separate studies. Baechler *et al* inkjet printed multi-walled carbon nanotube (MWCNT) electrodes onto cast silicone substrates to fabricate DEAs [54.] Anionic surfactant-treated MWCNTs were suspended in an alcohol-based solution, and the printed electrodes had a conductivity of up to 30 S cm^{-1} and exhibited self-clearing. Schlatter *et al* inkjet printed a mixture of Ketjenblack EC-300J carbon black, Wacker Besil® SPG 128 VP silicone surfactant, and OS-2 solvent to produce patterned DEA electrodes on blade-cast silicone substrates [55]. These DEA electrodes had a sheet resistance of 13–30 kΩ/square, and the DEAs exhibited an actuated strain of 8.8% at 94 V μm^{-1}. Kurian *et al* 3D-printed a MWCNT/Ecoflex 00-30 silicone composite electrode material, but it was extruded into vias for a stretch sensor rather than inkjet printed for DEAs [56].

We present below the materials and methods used to print thin patterned silicone membranes, their characterization, and the performance of DEAs made using these printed membranes.

2. Materials and methods for inkjet printing

2.1. Silicone ink preparation

In order to 3D print silicone membranes for DEs, silicone precursors were diluted in an appropriate solvent to produce an ink suitable for inkjet printing. As mentioned previously, one key advantage of this approach over existing inkjet printing technologies is the ability to print commercially available silicones and other elastomers. This gives access to the full range of electromechanical properties required of these materials, rather than having to compromise with printing pseudo-rubbers that jet easily but are not as electrically or mechanically robust. Standard silicones are available as two-component kits that are to be mixed in a certain ratio, then either thermally or UV cured. Seven commercially available silicone elastomer materials were investigated in this work, in which the first six are thermally curable, and the final one is UV curable: Wacker Elastosil® P7670, NuSil MED-4086, NuSil CF18-2186, Bluestar Silbione® LSR 4305, Wacker Silpuran® 6000/05, Wacker Elastosil® LR 3003/03, and Momentive Silopren® UV Electro 225-1.

During printing, silicone precursors remained inside the nozzle for extended periods of time. To safeguard against clogging the printing system due to crosslinking of the silicone, the two-component silicone elastomers were not mixed prior to dilution and subsequent printing. It was found that depositing a diluted component of part A, followed by a diluted component of part B directly on top, and then thermally curing resulted in silicone membranes with the same mechanical integrity as those mixed prior to dilution, then cast. Therefore, part A and part B of each of the six thermal cure silicones were diluted separately and printed independently, as two individual inks. The layers being only of order 1 μm thick, diffusive mixing between layers occurred very rapidly. Because the six thermal cure silicones are normally mixed in a 1:1 ratio of parts A–B, the same dilution ratio for the part A ink was used for the part B ink. The UV cure silicone initiator was mixed with the base prior to dilution since the mixture is only sensitive to high intensity UV radiation and not standard lighting. The recommended mixture for the UV silicone was a 50 to 1 ratio of the base to catalyst initiator. However, at the dilutions required, a ratio of 2 to 1 base to initiator was found to be ideal.

When designing inks for inkjet printing, the properties of interest are primarily viscosity and surface tension. In their undiluted form, all 13 silicone precursors have viscosities and surface tensions that are too high for printing. The printing system utilized (jetlab® 4, MicroFab Technologies, Inc.) recommends inks with viscosities in the range of 0.5–40 mPa s and surface tensions in the range of 20–70 mN m^{-1}. In addition to surface tension and viscosity, an ink with stable droplet formation free of satellites should have a Z value between 1 and 10, in which

$$Z = \frac{\sqrt{\gamma\rho\phi}}{\eta}, \tag{1}$$

where γ is the ink surface tension in air, ρ is the ink density, ϕ is the drop diameter, and η is the ink dynamic viscosity [57]. A Z value less than 1 will be too viscous to print, while a Z value greater than 10 will be too inviscid and will form multiple satellite droplets rather than single stable droplets [47]. For these calculations, it was assumed that the drop diameter was approximately the same as the nozzle diameter. A nozzle diameter of 80 μm was used exclusively throughout this paper, although the jetlab® 4 inkjet system is capable of printing with nozzle diameters that range from 20 μm up to 120 μm. Table 1 presents Z values calculated for only the 80 μm nozzle/drop diameter used in this study.

The 13 silicone precursors were diluted and the properties of viscosity, surface tension, and density of the resulting mixtures were measured. Viscosities were measured using a DV-II + Pro viscometer (AMETEK Brookfield), surface

Table 1. Summary of filtered silicone inks and their physical properties for DOD inkjet printing. The primary purpose of these measurements was to ensure that the formulations had a Z value between 1 and 10 prior to printing.

Prepared dilution (ratios given by weight)	Measured viscosity (mPa s)	Viscometer RPM	Measured density (g ml^{-1})	Measured surface tension (mN m^{-1})	Calculated Z, 80 μm drop diameter
2:1 OS-2:Wacker Elastosil® P7670, Part A	17.9	12	0.806	21.4	2.1
2:1 OS-2:Wacker Elastosil® P7670, Part B	13.5	20	0.832	21.4	2.8
4:1 OS-2:NuSil MED-4086, Part A	10.5	20	0.760	20.7	3.4
4:1 OS-2:NuSil MED-4086, Part B	8.52	20	0.809	21.0	4.3
4:1 OS-2:NuSil CF18-2186, Part A	10.5	20	0.807	21.2	3.5
4:1 OS-2:NuSil CF18-2186, Part B	9.38	20	0.796	21.4	3.9
5:1 OS-2:Bluestar Silbione® LSR 4305, Part A	9.78	20	0.850	20.9	3.9
5:1 OS-2:Bluestar Silbione® LSR 4305, Part B	10.2	20	0.800	20.9	3.6
6:1 OS-2:Wacker Silpuran® 6000/05, Part A	7.16	20	0.776	21.4	5.1
6:1 OS-2:Wacker Silpuran® 6000/05, Part B	5.93	20	0.768	21.1	6.1
7:1 OS-2:Wacker Elastosil® LR 3003/03, Part A	7.43	20	0.754	21.7	4.9
7:1 OS-2:Wacker Elastosil® LR 3003/03, Part B	6.36	20	0.755	21	5.6
4:1 OS-2:Momentive Silopren® UV Electro 225-1 (base:initiator 2:1)	17.8	12	0.771	21.7	2.1
Pure Deionized Water, 20 °C (measured)	1.33	150	1.004	70.8	—
Pure Deionized Water, 20 °C (reference)	1.0	—	1.0	72.8	—

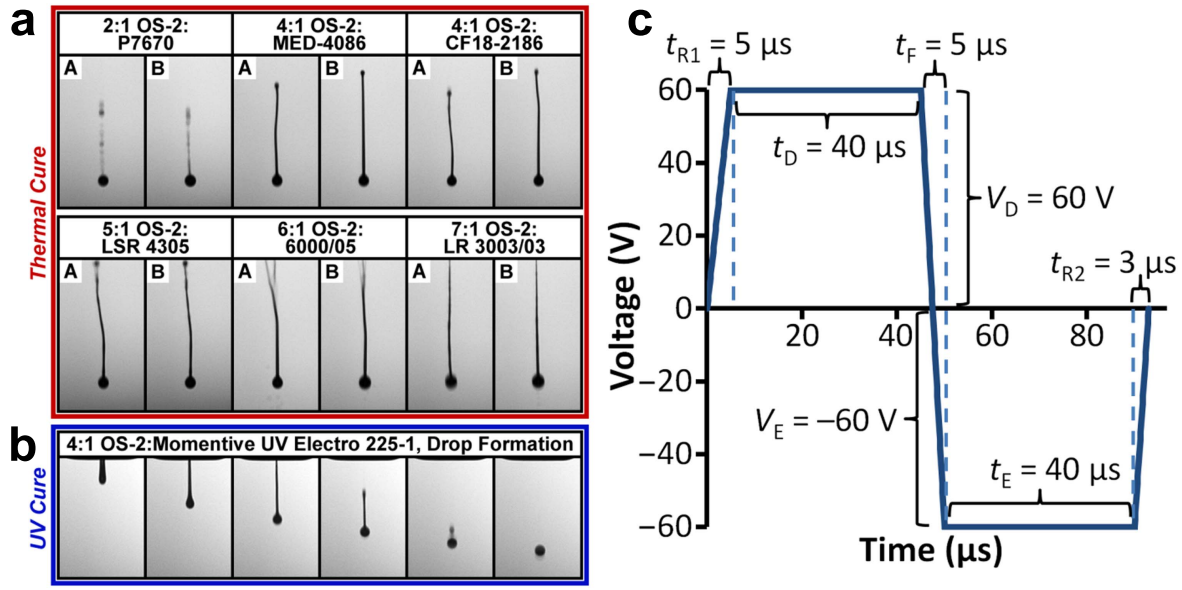

Figure 1. (a) High-speed stroboscopic photographs of jetting droplets formed for six two-component thermal cure silicone elastomer inks, consisting of the precursors diluted in the ratios of Dow Corning® OS-2 shown. A strobe delay has been applied to some of the photographs so that the droplet appears in approximately the same position for all. (b) Drop evolution of UV cure ink consisting of Momentive Silopren® UV Electro 225-1 precursor diluted in four parts OS-2. Each still is separated by a strobe delay of 100 μs, effectively representing the chronological progression, from left to right, of drop formation as it falls. The drop is first ejected from the nozzle with a long tail, which eventually coalesces with the drop body and results in a single droplet before hitting the substrate. (c) Jetting waveform and specified parameters utilized for all thermal and UV cure silicone inks: dwell voltage (V_D) = 60 V, echo voltage (V_E) = −60 V, rise time 1 (t_{R1}) = 5 μs, dwell time (t_D) = 40 μs, fall time (t_F) = 5 μs, echo time (t_E) = 40 μs, rise time 2 (t_{R2}) = 3 μs, and idle voltage (V_I = 0 V). Backpressure varied from −12 to −20 mbar. These parameters were chosen to achieve stable droplets with minimal satellite formation, independent of frequency. These same jetting parameters were applied for all photographs in this figure.

tensions were measured with an AquaPi surface tensiometer (Kibron, Inc.), and densities were measured using an autopipette and digital laboratory scale. The solvent used for all 13 silicone inks was Dow Corning® OS-2. The minimum amount of OS-2 solvent was chosen such that the viscosity, surface tension, and Z value all lay within the printable ranges given above. Once the appropriate dilutions were found, all inks were passed through a syringe filter with a pore size of 1 μm prior to measuring viscosity, surface tension, and density. Filtering is an important step to prevent clogging of the nozzle prior to printing, either from any contaminants, or from polymer chains or other ink components that are too large. Table 1 summarizes the chosen filtered silicone ink formulations and their measured physical properties. Deionized water was measured and compared to reference standards; the measured viscosity was 33% higher than the reference value. For the purpose of finding dilutions that fall within given ranges, this amount of deviation was not a concern.

2.2. Waveform design and jetting profiles

The jetlab® 4 DOD inkjet printing system allows custom inks to be printed by providing control of nozzle size, waveform design, and backpressure, and by incorporating a camera with high-speed stroboscopic illumination to monitor droplet formation. In addition, the piezoelectric nozzle actuator allows jetting of both aqueous and organic solvent-based inks, the latter of which is of particular interest to printing silicones in OS-2. The design of the drop ejection waveform is important to ensure stable droplet formation and jetting of the ink, and so careful attention was paid toward its development. For stable jetting of most materials, a bipolar waveform with a positive and a negative component is recommended and was therefore utilized.

Increasing the ejection voltage of the nozzle piezoelectric actuator increases the droplet ejection force and is known as the dwell voltage (V_D), represented by the positive amplitude of the waveform (figure 1(c)). Increasing the time interval that V_D is active per cycle has a similar effect on improving droplet ejection, and this time interval is known as the dwell time (t_D). For bipolar waveforms, the negative amplitude is called the echo voltage (V_E), and the corresponding 'on' time is the echo time (t_E). The parameters V_D, t_D, and t_E were increased and V_E was decreased until stable jetting was achieved. Because a symmetric waveform worked best for the silicone inks, t_D and t_E were both kept equal and were increased together, and the magnitude of V_D was kept equal to and increased in tandem with the magnitude of V_E. The rise and fall times (t_{R1}, t_{R2}, t_F) were then altered slightly to fine tune the droplet formation, while being kept as low as possible. All silicone elastomer films and 3D structures printed in this work utilized the same jetting parameters shown in figure 1(c). Only the backpressure was altered for each ink to values between −12 and −20 mbar, such that the effect of gravity would be offset and the ink meniscus would be approximately level with the nozzle edge. As the waveform illustrates, the following jetting parameters were utilized:

$V_D = 60$ V, $V_E = -60$ V, $t_{R1} = 5\ \mu$s, $t_D = 40\ \mu$s, $t_F = 5\ \mu$s, $t_E = 40\ \mu$s, $t_{R2} = 3\ \mu$s. The waveform was symmetric about the horizontal axis, so the idle voltage (V_I) was 0 V.

This same jetting waveform was used to print droplets for all 13 silicone inks, as pictured in figures 1(a) and (b). These jetting profiles were photographed with a high-speed stroboscopic backlight synced with or at a slight phase delay to the jetting frequency of 2 kHz, although the same droplet profiles were observed for lower frequencies as well. All the silicone ink droplets had tails, a common non-Newtonian feature for polymer-based inks that have medium to high molecular weights [57–62]. As seen in figure 1(a), the tail features of parts A and B for any given ink are very similar, implying a similar molecular weight and composition. The P7670 ink had the least pronounced tail of the 12 thermal cure inks, while the 6000/05 had one of the longest tails, which had split into several branches. In all cases, the drop tail eventually merged with the droplet prior to, or shortly following, contact with the substrate. This is evidenced in figure 1(b), which depicts the droplet formation and evolution for the one-part UV 225-1 ink. The sequence was created by increasing the strobe light delay in increments of 100 μs. For this ink, the tail is observed to eventually coalesce with the drop body, until a spherical droplet with no tail is visible, as seen in the far right frame.

2.3. From drops to solid membranes

DOD inkjet printing jets only when needed, rather than continuously [62]. By doing this, DOD printing can place drops in predefined positions, giving precision down to the drop level. The jetlab® piezoelectric printing system offers two DOD print modes. In the first mode, a drop or a series of drops is placed in a single location, and only then is the stage moved relative to the nozzle to the next position. However, this higher precision printing option can be time-prohibitive for larger areas. Therefore, a less precise but still high-resolution process called printing on-the-fly was utilized for all 3D-printed structures in this paper. In this second print mode, the stage moves continuously with respect to the nozzle for each line at a specified speed, and for arrays the drops are jetted at a certain frequency that is calculated by the specified drop spacing. Because there is no stage acceleration during the printing of a line, nor is there any change in the frequency, the drops are placed on the substrate at a constant spacing with high precision. To further save time in the print on-the-fly mode, the line can raster back and forth during bidirectional printing. While still precise, bidirectional printing can create a slight drop offset between adjacent rows, which may be undesirable for printing some higher resolution lines and edge features. Precision can further be increased if the nozzle is very close to the substrate to limit the droplet fly time. For the structures printed in this paper, sufficient precision was obtained by printing on-the-fly, bidirectionally, and with a nozzle tip-to-substrate distance of 3.2 mm.

Figure 2 summarizes the effect of drop spacing on printed film quality. The single-component Momentive 225-1 UV-cure silicone elastomer was printed on-the-fly at 50 mm s^{-1}, bidirectionally, while the drop spacing was sequentially halved from 400 μm down to 50 μm in both the horizontal and vertical directions. This is equivalent to sequentially doubling the number of drops per 10 mm side from 25 drops/side up to 200 drops/side. Input of either drop spacing or drops per side into the printer control software will print the same pattern and sequence. From these inputs, the printer calculates the required jetting frequency f when printing on-the-fly based on the following formula:

$$f = \frac{v}{\lambda} = \frac{v}{l/n}, \tag{2}$$

in which the fly speed v is divided by the drop spacing λ, which in turn equals the side length l divided by the number of drops per side n. For example, at a specified drop spacing of 400 μm (25 drops per 1 cm side) and a print on-the-fly rate of 50 mm s^{-1}, the jetting frequency is: (50 mm s^{-1})/(0.4 mm) = 125 Hz. Hence from the point of view of the printer, all other jetting parameters remained constant while the jetting frequency was doubled from 125 Hz up to 1.0 kHz to produce the patterns in figure 2. As seen in figure 2(a), at a drop spacing of 400 μm in both the horizontal and vertical directions, individual drops are visible as they do not yet coalesce. The average height of each deposited drop was 0.30 μm (standard deviation σ: 0.13 μm, number of data points: 1.13×10^6). Here, 'data points' refer to all non-zero thickness values taken from the color-coded thickness images shown in figure 2. These thickness images were measured using a Veeco WYKO NT1100 white light interferometer. Due to the bidirectional print setting, a slight offset between rows is apparent at this wide spacing. Also, the drops at the edges appear to be slightly taller and have slightly smaller diameters than the other drops in each row. This is likely due to the 1–2 s pause between printing rows that results in some solvent evaporating from the material in the nozzle prior to printing the next row.

In some cases, a pattern with individual drops may be desired, such as in texturing a surface, but for creating solid membranes the spacing should be decreased. Halving the spacing to 200 μm in both directions begins to create some overlap, but the rows and even individual drops are still visible. At this point, the offset between rows is no longer apparent. The surface texture is rough, and the average thickness is 0.71 μm (σ: 0.16 μm, 2.25×10^6 data points). Halving the spacing once more to 100 μm in each direction now results in a continuous, high-quality silicone film with well-defined edge features. The surface texture is also very smooth, with an average thickness of 2.8 μm (σ: 0.15 μm, 2.25×10^6 data points). Finally, at a horizontal and vertical spacing of 100 μm, the drop density is too high and too much material is printed. The result in this case is a low quality film with poorly defined edge features and an uneven thickness of at least 7.4 μm on average (σ: 1.64 μm, 1.95×10^6 data points). The average and standard deviations for this final sample may in fact be higher due to some uncollected data (white areas) that were outside the scanning window. However, the conclusion remains that the film was thicker and less uniform.

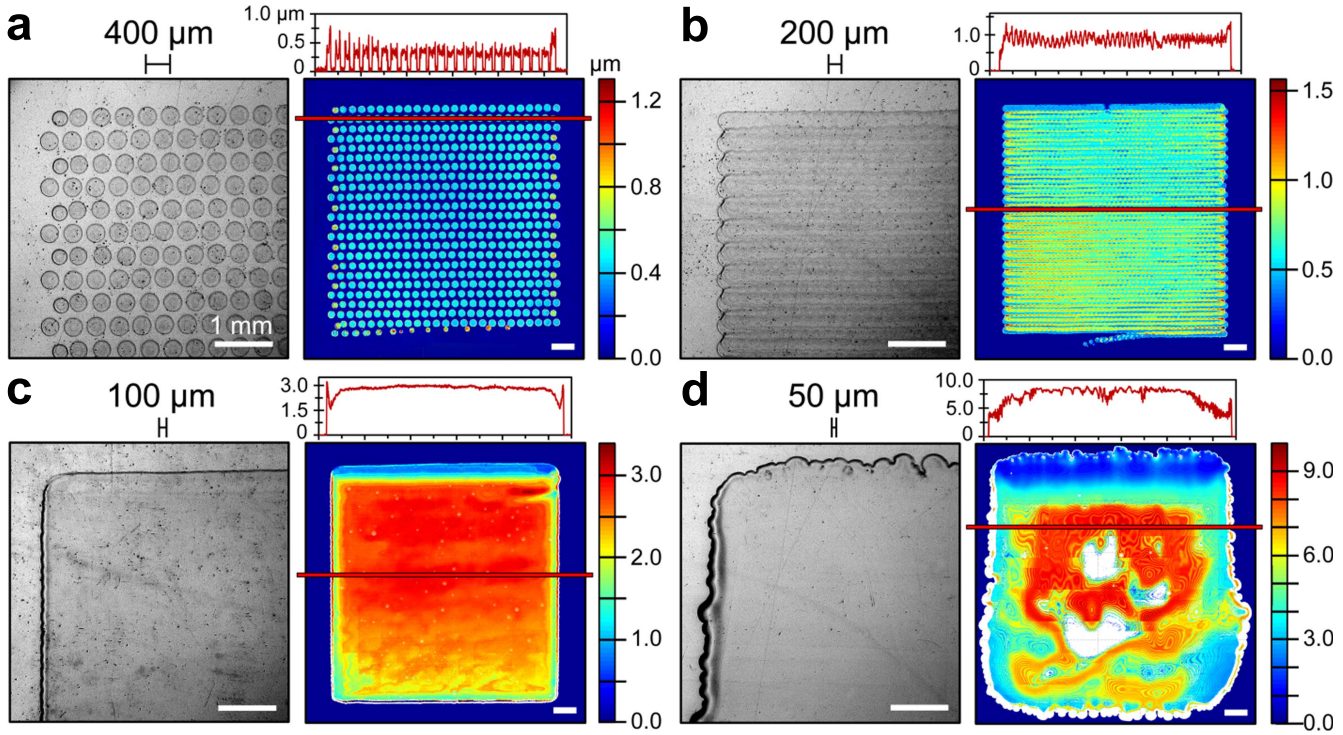

Figure 2. The effect of drop spacing on printed film quality using the Momentive 225-1 UV-cure silicone elastomer on glass substrates. The films were printed on-the-fly at 50 mm s^{-1}, bidirectionally, while the drop spacing was sequentially halved from 400 μm down to 50 μm in both the horizontal and vertical directions. Shown at left are optical micrographs, at right are the corresponding optical surface profiles, and above are the cross-sections taken at the level indicated by the red horizontal lines. All thicknesses and topological features are in micrometers, and all scale bars equal one millimeter. Each printed area is 1 cm^2. (a) At a drop spacing of 400 μm, individual drops are visible but do not coalesce. The average drop height is 0.30 μm. An offset is visible and drops are higher at the edges due to the bidirectional (back-and-forth) printing pattern. (b) At a spacing of 200 μm, the average thickness is 0.71 μm, and the drops are beginning to overlap. (c) At a spacing of 100 μm, the drops have completely overlapped to form a silicone film of optimal quality with an average thickness is 2.8 μm. (d) At a spacing of 50 μm, too much material is printed and a poor-quality film is produced with a mean thickness of 7.4 μm.

It should be noted that the effect of drop spacing on film quality will vary with the type of material printed, as well as with the nozzle diameter. For the Momentive UV Electro 225-1 and the 80 μm nozzle diameter used exclusively throughout this paper, the optimal drop spacing is near 100 μm. However, the optimal drop spacing for the other silicones was found to vary. These optimal spacings, or values close to them, were chosen when printing the various silicone membranes depicted in figure 3. The optimal drop spacing is a qualitative measure, chosen such that neither too much material is printed such that films have uneven thicknesses or poorly defined features, nor too little material is printed such that the drops do not coalesce or the resulting films are too rough. In addition, the OS-2 solvent evaporated quickly for all tested silicone inks, and the films were dry and non-tacky to the touch prior to taking thickness measurements.

3. Characterization techniques

3.1. Mechanical testing

The stress–strain measurements presented in figure 4 were produced as follows. Prior to printing silicone film samples for mechanical testing, a substrate of polyethylene terephthalate (PET) coated with a sacrificial layer of poly(acrylic acid) (PAA) was prepared. A ~5% solution of PAA was formulated by mixing one part 25 wt% 50 kDa PAA in deionized water with four parts isopropanol. The PAA solution was then blade-cast onto a ~115 μm thick PET foil with a blade-to-PET gap width of 85 μm and a speed of 25 mm s^{-1}. The IPA and water is then left to evaporate.

Next, silicone membranes with an area of 12.5 mm × 25 mm were printed onto the PAA/PET substrates. The Momentive UV Electro 225-1 ink was printed on-the-fly at 50 mm s^{-1} and 475 Hz, depositing drops with a spacing of 105.3 μm in both the vertical and horizontal directions, giving a printed resolution of 95 drops/centimeter (dpc) or 241 drops/inch (dpi). Curing was performed with a 60 W, 365 nm peak-wavelength Pro-Ma UV Exposure Unit for 12 min, however cure times less than 2 min are possible with a higher intensity UV source, such as 1 kW. The CF18-2186 ink, part A, was printed on-the-fly at 50 mm s^{-1} and 450 Hz, depositing drops with a spacing of 111.1 μm in both the vertical and horizontal directions, giving a printed resolution of 90 dpc or 229 dpi. The same was settings were applied to part B, which was printed directly on top of part A. Interestingly, diffusion through these small thicknesses allows for sufficient mixing

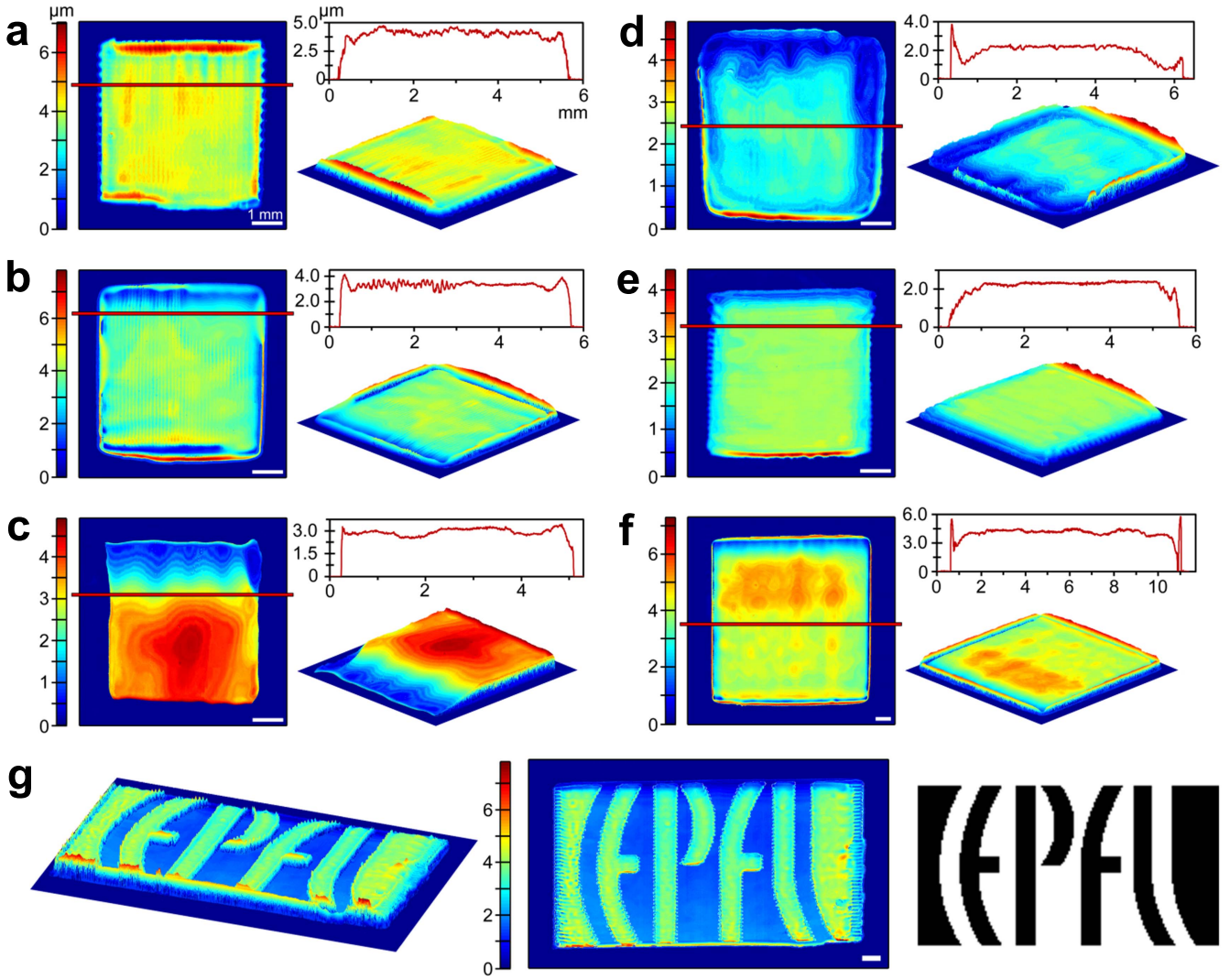

Figure 3. Surface morphology of 3D-printed silicone elastomer membranes on glass, imaged via optical profile interferometry. The cross-sections were taken at the level indicated by the horizontal red lines. (a)–(d) and (f) are thermal cure silicone elastomers in which part A was printed first, followed by part B that was printed directly on top, and finally thermally cured. (e) and (g) were cured using a UV source. All thicknesses and topological features are in micrometers, and all scale bars equal one millimeter. (a) 5 mm × 5 mm Wacker Elastosil® P7670 with an average thickness of 4.1 μm, printed on-the-fly with a drop spacing of 151.5 μm at 330 Hz (33 drops in x and in y, or 168 dpi). (b) 5 mm × 5 mm NuSil CF18-2186 with an average thickness of 4.0 μm, printed with a drop spacing of 111.1 μm at 450 Hz (45 × 45 drops, 229 dpi). (c) 5 mm × 5 mm Bluestar Silbione® LSR 4305 with an average thickness of 3.7 μm, printed with a drop spacing of 100.0 μm at 500 Hz (50 × 50 drops, 254 dpi). (d) 5 mm × 5 mm Wacker Silpuran® 6000/05 with an average thickness of 2.0 μm, printed with a drop spacing of 166.7 μm at 300 Hz (30 × 30 drops, 152 dpi). (e) 5 mm × 5 mm UV-cure Momentive Electro 225-1 with an average thickness of 2.3 μm, printed as one layer with a drop spacing of 104.2 μm at 480 Hz (48 × 48 drops, 244 dpi). (f) 10 mm × 10 mm NuSil CF18-2186 with an average thickness of 4.5 μm, printed with a drop spacing of 111.1 μm at 450 Hz (90 × 90 drops, 229 dpi). (g) 10 mm × 18.4 mm 3D-printed EPFL logo of Momentive UV Electro 225-1. Consists of a 2 μm base layer and a 2 μm text layer, each printed on-the-fly with a drop spacing of 100 μm at 500 Hz. The text layer was printed from the monochrome bitmap at right.

part B into part A prior to curing. The resulting membrane was then cured at 80 °C in an oven for 60 min.

The printed and cured elastomer films were then affixed to sample holders using double-sided tape. A silicone sample under test and this sample holder are pictured in figure 4(d). An area of 12.5 mm × 25 mm was chosen to allow for a 5 mm margin on the top and bottom of the sample to affix to the double-sided tape, leaving a test area of 2.5 mm × 25 mm, a 1:10 ratio. Finally, the substrate, film and holder were submerged in boiling deionized water to dissolve the PAA layer and release the silicone film and its holder.

For comparison, the same materials were blade-cast onto the PAA/PET substrate to create control groups. The unaltered 4:1 OS-2:Momentive UV Electro 225-1 ink was blade-cast onto the PAA/PET at 15 mm/second using a 150 μm total blade gap. For the 4:1 OS-2:CF18-2186 ink, both part A and part B were mixed prior to blade casting, using the same gap and speed settings as above for the 225-1. The cast films were then UV and thermally cured, respectively, using the same curing settings above. 12.5 mm × 25 mm rectangles of silicone/PAA/PET were laser cut out of the larger substrate and affixed to the PI tape on the PMMA holders. The control

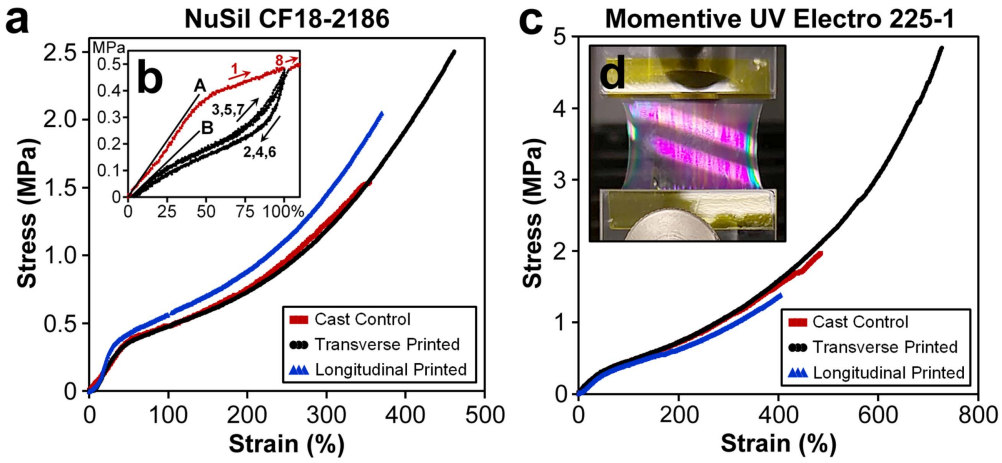

Figure 4. Tensile nominal stress–strain curves for inkjet 3D-printed and blade-cast (control) silicone membranes, at a pull rate of 10 mm min^{-1}. The printed membranes had either a raster parallel to the pull axis ('transverse') or perpendicular to the pull axis ('longitudinal'). A slight discontinuity exists at 100% strain for all curves because cyclic data was collected in the middle of the tensile test, before pulling to failure. (a) For NuSil CF18-2186, the UTS and maximum elongation were 1.54 MPa and 355%, 2.5 MPa and 462%, and 2.05 MPa and 370% for the blade-cast control, transverse printed, and longitudinal printed membranes, respectively. Sample thicknesses were: 2.35 μm (control), 4.33 μm (transverse printed), and 4.51 μm (longitudinal printed). (b) Cyclic data (black) for CF18 Cast Control at 10 mm min^{-1}, overlaid on stress–strain curve (red). Cyclic testing was performed to compensate for the Mullins effect during Young's modulus calculation, in which the slope at 0% strain decreases from A (790 kPa) to B (710 kPa). A total of four loading-unloading cycles (8 steps, indicated by the arrows) were performed before rupture. (c) For Momentive UV Electro 225-1, the UTS and maximum elongation were 1.97 MPa and 485%, 4.84 MPa and 727%, and 1.39 MPa and 405% for the control cast, transverse printed, and longitudinal printed membranes, respectively. Sample thicknesses were: 2.35 μm (control), 2.23 μm (transverse printed), and 2.35 μm (longitudinal printed). (d) Photograph of a suspended membrane under test at 600% strain just prior to rupture. Thin-film interference caused the primarily purple hue, which changed color as the thickness changed during the pull test.

films were released using the same boiling deionized water procedure above.

To test the mechanical performance, the samples and holders were loaded onto an Instron® testing system. An outer PMMA frame that was holding both sides of the sample holder at a fixed distance was then removed. A tensile test was performed to determine the general shape of the stress–strain curve and find the maximum elongation at failure. A cyclic test was also performed prior to failure to determine the Young's modulus at 0% strain, as the slope decreases with repeated extensions and relaxations, known as the Mullins effect [63]. Specifically, the test consisted of a pull test at a rate of 10 mm min^{-1} (0.17 mm s^{-1}) to 100% strain, followed by a cyclic test cycling between 0% and 100% strain for six legs at the same rate, and finally a pull test from 100% strain up to rupture at the same rate. This is depicted in figure 4(b). Printed samples were tested in two distinct orientations: the 'transverse' direction where the print direction was across the length of the sample or parallel to the pull axis, and 'longitudinal' in which the print direction was along the length of the sample or perpendicular to the pull axis.

Force, displacement, and time were measured by the Instron®. The initial thickness of each sample was measured using white light interferometry (Ocean Optics USB4000-VIS-NIR), in which a measurement was taken in three locations and then averaged. The nominal stress σ_N was then calculated, defined as

$$\sigma_N = \frac{F}{A_0} = \frac{F}{t_0 w_0}, \tag{3}$$

where the measured tensile force F was divided by the initial cross-sectional area A_0, which equals the product of the measured average initial thickness t_0 and the known initial width w_0 of 25 mm. For simplicity, the nominal stress was calculated rather than the true stress, which takes into account how the thickness changes with elongation. This is because the true thickness was not homogeneous across the sample during tensile elongation, as evidenced by the bowing catenary structures on both sides of each sample, as well as by the multiple thin film interference colors. Next, the strain was calculated as simply the percent change in the displacement measurement. The results are given in figures 4(a) and (c).

Next, the Young's modulus was calculated from the slope of the tangent line at 0% strain. Due to the Mullins effect, there was often a non-negligible reduction in this slope with cycling. Therefore, tangents were measured for the final three cycling curves, after the slope had decreased. For each test, there were four rising curves from 0% to 100% strain, labeled as 1, 3, 5, and 7 in figure 4(b). Curve 1 usually had a higher 0% tangent slope, while curves 3, 5, and 7 would all typically have lower slopes and were very close to one another in value. To calculate the 0% tangents, the stress–strain data was fit with a line from 0% to 0.25% strain and the slope was measured. The slopes of the 0% tangents for curves 3, 5, and 7 were averaged together for each silicone sample trial. Then, these trial averages were averaged together to obtain a mean for each group, and the standard error was calculated. Finally, the ultimate tensile strength (UTS) and percent elongation at failure for each sample trial were averaged together and the standard error was calculated

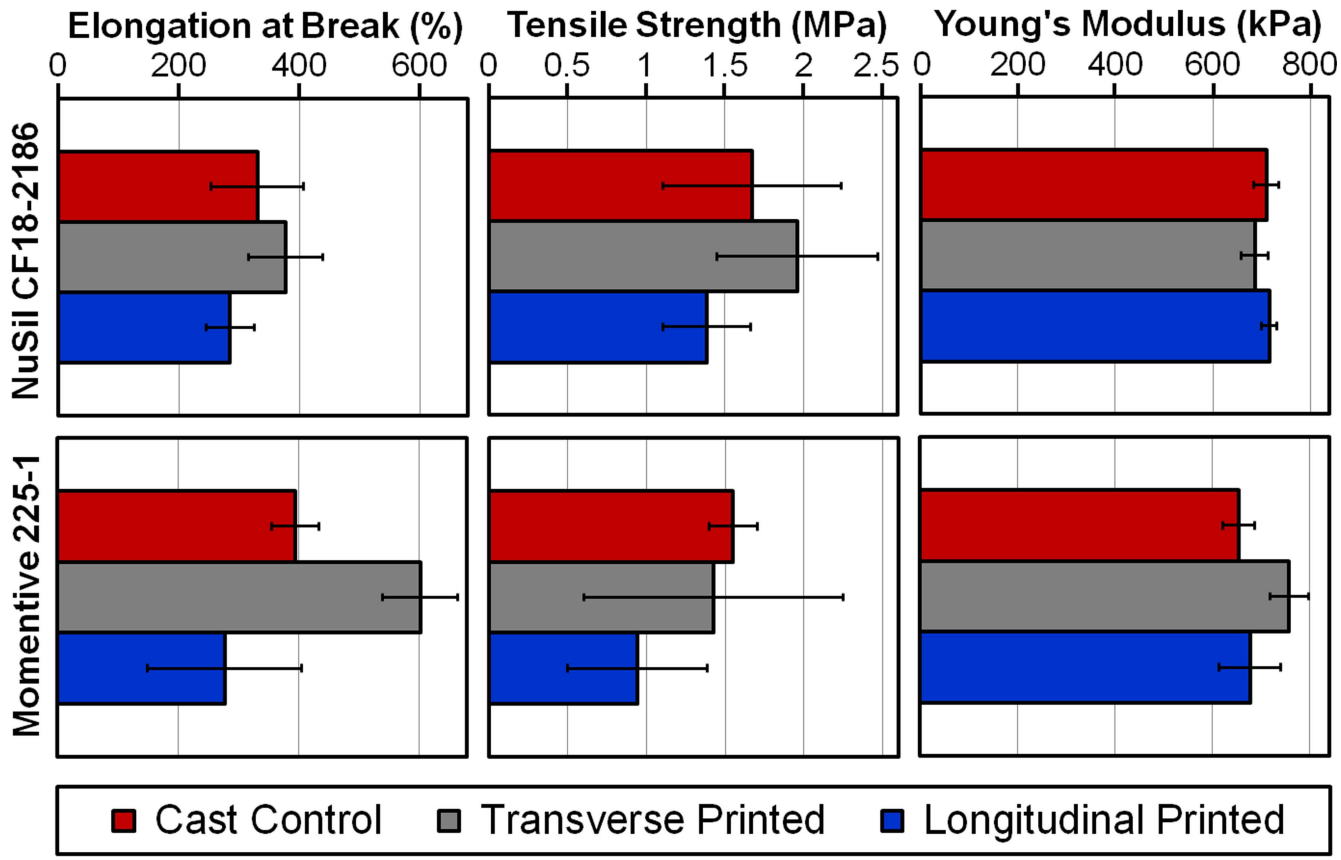

Figure 5. Mean statistics for maximum elongation at break, ultimate tensile strength, and Young's modulus for the blade-cast control, transverse printed group, and longitudinal printed group. Data are shown for the thermal cure NuSil CF18-2186 and the photocure Momentive UV Electro 225-1 silicone elastomers. For all CF18 properties, there is no statistically significant difference among mean groups due to the overlap of the standard error bars. The same applies for the tensile strength among all groups for the 225-1. Although the standard error bars do not overlap for the 225-1 Young's modulus Cast Control and Transverse Printed groups, the difference is not statistically significant (unpaired t test, $P = 0.101$). However, the difference is statistically significant between the means of the 225-1 Elongation at Break Cast Control and Transverse Printed groups (unpaired t test, $P = 0.008$).

within each group. These results are plotted in figure 5, in which the error bars represent plus or minus one standard error from the mean.

3.2. Printed DEA fabrication and testing

Actuator silicone samples were printed on the same PAA-coated PET substrates used for the mechanical testing, described above in section 3.1. A monochrome bitmap image was used to print circles of Momentive UV Electro 225-1 and of CF18-2186, both with a diameter of 2 cm and a drop spacing of 100 μm. This resulted in a printed resolution of 100 dpc, or 254 dpi. As before, the 225-1 was UV-cured for 12 min at 60 W and 365 nm peak wavelength, and the CF18-2186 was printed part B atop part A and then thermally cured at 80 °C for 60 min. Control groups of 2 cm circles were laser cut from the same cast membranes of 225-1 and CF18-2186 on PAA/PET used for the control groups of the mechanical tests described in section 3.1. Electrodes of a standard ink were pad-printed onto all silicone circles using a cliché pattern with a 2 mm diameter active area (~2.4 mm after prestretch) [5]. The standard ink consisted of 0.8 g of carbon black (AkzoNobel, Ketjenblack® EC-300J) ball mixed with 4 g each of parts A and B of Bluestar Silbione® LSR 4305 in 16 g of isopropanol and 16 g of isooctane.

Next, via an approach similar to that used by Poulin *et al*, the silicone was released from the substrate [52]. Specifically, laser-cut PET rings lined with ARclear® adhesive (Adhesives Research, 8932EE) were affixed to the circles. Then, the PET/ARclear®/silicone/PAA/PET system was submerged in boiling deionized water, which dissolved the PAA, releasing the PET/ARclear®/silicone from the PET substrate. The PET/ARclear® rings holding the silicone were left to dry, and were then mounted to a radial prestretching apparatus. A radial prestretch of roughly 20% was applied to all silicone circles, which were previously pad-printed with electrodes. Then an ARclear®-lined PMMA frame with an inner diameter of 1.0 cm was affixed to the prestretched silicone, and the silicone outside the frame was cut to release it from the prestretcher. The frames were affixed to the samples on the pad-printed side, which also provided an electrical contact between the electrode via and conductive tape affixed to the frame. To complete fabrication, two prestretched silicone membranes of the same material on circular frames on opposite sides were brought together in direct silicone-silicone contact, ensuring the pad-printed electrode circles

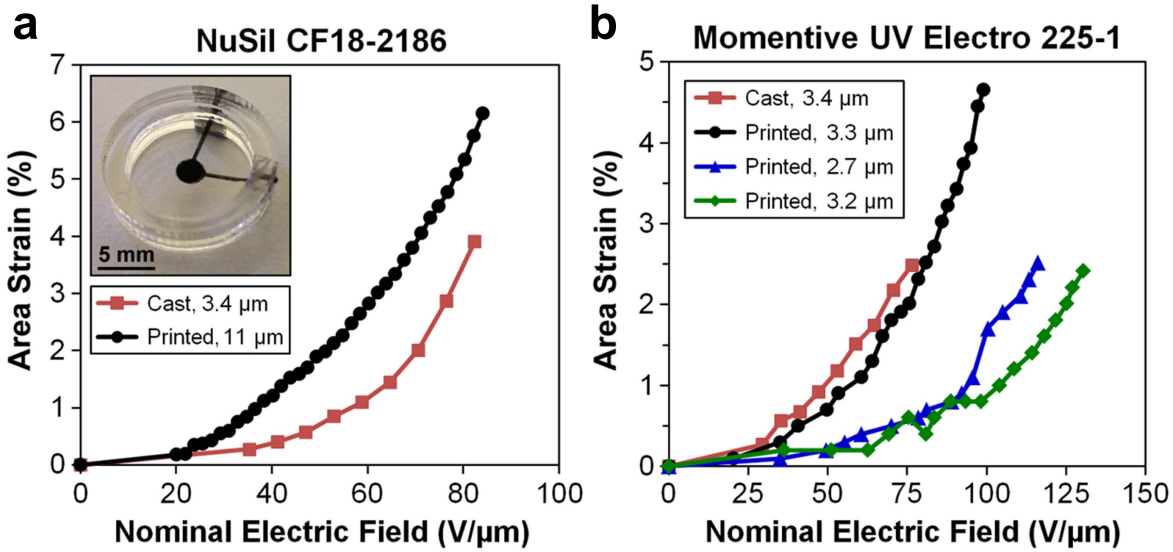

Figure 6. Actuation performance of inkjet 3D-printed silicone membranes with pad printed electrodes (black, green, and blue curves), and blade-cast control silicone membranes with pad printed electrodes (red curves). The dimensions given in the legends are the thicknesses of the dielectrics. (a) Actuation area strain in percent as a function of the nominal electric field for NuSil CF18-2186 thermally cured silicone elastomer. A maximum strain of 6.1% at 84.0 V μm^{-1} was reached by a DEA with the inkjet printed elastomer. This was comparable to the blade cast control that reached 3.9% strain at 82.4 V μm^{-1}. *Inset:* photograph of a completed expanding circle DEA under test with 3D-printed silicone membranes and pad-printed electrodes. (b) Actuation of the Momentive UV Electro 225-1 photocured silicone elastomer. Three different DEAs with inkjet printed dielectrics showed a variation in performance ranging from 4.7% maximum area strain at 99 V μm^{-1} (black curve) to 2.4% strain at 129.6 V μm^{-1} (green curve). These actuators shared certain metrics with the blade-cast control DEA, which achieved 2.5% maximum area strain at 76.5 V μm^{-1}.

overlapped correctly. The resulting DEA is pictured in the inset in figure 6(a).

Thicknesses of the prestretched DEAs were determined via white light interferometry using the same method described in section 3.1. The DEAs were tested using an in-house, regulated high voltage power supply as the input [64], and the actuation strain response was recorded using a USB microscope. Input voltages were incrementally increased by steps of 20 V from 0 V up to complete dielectric breakdown, in which an actuation strain response is no longer recorded for a non-zero input voltage. Stills were captured of each actuation event from the recorded video. The contrast was increased by the same amount in all the stills, and the black electrode pixel area was measured for each still. The percent change in electrode area of each active still compared to the 0 V stills gave the percent increase in area with voltage. In addition, in-house motion tracking software was utilized to track the actuation strain of the three UV inkjet printed DEAs in figure 6(b).

Throughout this study, nominal electric field is utilized for simplicity, which is defined as

$$E_N = \frac{V}{t_0}, \tag{4}$$

where the applied voltage V is divided by the measured initial thickness after prestretch t_0. The actuation performance presented with the nominal electric field is given in figure 6.

4. Results and discussion

4.1. Printing silicone rubber and 3D structures

A total of seven silicone elastomer materials have been investigated for printing in this work: six two-part thermal cure silicone elastomers and one UV cure silicone elastomer. This makes a total of 13 silicone ink preparations whose jetting properties were investigated. As noted in section 2.1, all inks were filtered with 1 μm pore size syringe filters to remove long chains and particulates that may cause clogging. Of the seven materials above, both parts of the MED-4086 and LR 3003/03 inks were very difficult to filter. Although small volumes could be filtered to produce jetting results for these two materials (4 inks), it became impractical for printing solid structures. For this reason, and because it produced similar results to the other materials, the MED-4086 and the LR 3003/03 were eliminated. The remaining five materials considered for further study were: Wacker Elastosil® P7670, NuSil CF18-2186, Bluestar Silbione® LSR 4305, Wacker Silpuran® 6000/05, and Momentive Silopren® UV Electro 225-1. Figure 3 contains samples of the printing results of these five silicone elastomers.

The first five silicone thin films in figures 3(a)–(e) had a printed area of approximately 5 mm × 5 mm, which varied slightly depending on the properties of the ink utilized. In addition, figures 3(a)–(d) and (f) show thermal-cure silicone elastomers in which part A was printed first, followed immediately by part B which was printed directly on top of part A as a second layer. At these small thicknesses, diffusion allows for sufficient mixing of part B into part A, and the

printed membrane is then cured at 80 °C in an oven for 60 min, or on a hotplate at 150 °C in only 30 s. The UV-curable Momentive Electro 225-1 shown in figures 3(e) and (g) has only one component, and therefore can be printed in only one layer. This allows for faster print times and a potentially higher precision. Curing was performed at 60 W, 365 nm for 12 min, as described in section 3.1. Table 2 reports the average thickness, thickness standard deviation (σ), and other properties for the inkjet printed silicone membranes in figure 3. The thickness standard deviation can be interpreted as a general measure of the surface roughness.

The film in figure 3(e) was printed with a drop density of 96 dpc instead of the 100 dpc used in figure 2(c), although at 96 dpc the edges appear slightly less smooth due to less overlap between rows. The sixth printed film in in figure 3(f) utilized the same parameters as for the second NuSil CF18-2186 film but was four times the area at 10 mm × 10 mm. This film was printed using the same material inks and parameters as the second 0.5 cm × 0.5 cm film in figure 3(b), but at 1 cm^2 it had four times the area. A good-quality film of comparable thickness could be printed at this larger 1 cm^2 area, and the surface profile only appears to have better edge definition since it is viewed at the same size as the 0.5 cm × 0.5 cm film. All of these printed samples exhibit varying degrees of the 'coffee stain' effect, in which capillary flow causes a small amount of material to be pushed to the perimeter during drying to form a ridge [65]. These ridges are visible in the cross-sections of figures 2 and 3. In most cases, this ridge is of negligible height compared to the total printed membrane height.

The manufacturing approach presented in this work has the potential to create complex and precise three-dimensional structures including integrated active elements such as DEAs. To demonstrate the feasibility of printing 3D architectures in silicone elastomer, a two-layer structure of our institution logo including the letters 'EPFL' was 3D-printed in Momentive Electro 225-1 UV-curable silicone on glass, shown in figure 3(g). A rectangular base layer of dimensions 10 mm × 18.4 mm × ∼2 μm was first printed from a monochrome bitmap of a rectangle, with a drop spacing of 100 μm. It was printed on-the-fly at 50 mm s^{-1} and a 500 Hz jetting frequency, resulting in a resolution of 100 dpc or 254 dpi. The rectangular square was then UV cured for 12 min at 60 W and 365 nm peak wavelength. Next, the 'EPFL' logo text was printed in a second layer of silicone directly on top of the cured silicone rectangle, again from a monochrome bitmap. The second text layer had the same dimensions and thickness as the first layer, and was printed using the same settings as the first layer. The entire structure was UV cured once again under the same conditions. The resulting 3D structure was ∼4 μm thick with well-defined edge features and a relatively smooth surface morphology.

Of the six square thin films printed, those with the best quality were printed from Momentive UV Electro 225-1 (figure 3(e)) and NuSil CF18-2186 (figures 3(b) and (f)). These films had the smoothest surface features, the most well-defined edges, and the most homogenous thicknesses. Because they were the most reliable, they were chosen for the mechanical and actuation studies, detailed in the following sections. The second-best results were printed from Wacker Elastosil® P7670 (figure 3(a)), although the surface is slightly rougher and the edges are not as well-defined, as well as from Bluestar Silbione® LSR 4305 (figure 3(c)), which had a smooth surface but a slightly uneven thickness. These materials are also well-suited for most applications where a good resolution is required. For the printing parameters we used, Wacker Silpuran® 6000/05 films (figure 3(d)) had poorly defined edge features and an uneven thickness. Regardless of the drop spacing, this material either resulted in films with rough edges or the drop overlap was insufficient to form a smooth membrane. Note that when printed, this ink had one of the longest droplet tails that often bifurcated (figure 1(a)). This corresponds to the high molecular weight of the polymer, which also gave a high pot viscosity prior to ink formulation. This material can produce acceptable print results when a highly extensible silicone rubber is necessary for the application, but a high resolution is not required.

4.2. Mechanical performance

As mentioned just above, the two out of the five total materials chosen for further study were the Momentive Silopren® UV Electro 225-1 and NuSil CF18-2186. In addition to having good print results, the 225-1 was selected because it is the only UV-curable silicone tested, and the CF18-2186 was chosen to represent the two-component thermally curable silicone rubbers. Tensile and cyclic test results for both of these two materials are reported in figure 4. Two printed experimental groups and one blade-cast control group were compared for each material. The best performing groups are plotted in figure 4, while mean statistics of several trials within each group are presented in figure 5. Both experimental groups were inkjet printed with the parameters detailed in section 3.1, such that one group was printed transverse to the length (or parallel to the pull direction) and the other group was printed longitudinal to the length (perpendicular to the pull direction). The control group was blade-cast using standard protocol as described in section 3.1.

As shown in figure 4, the shape of the nominal stress–strain curve is essentially identical for each group consisting of the same material, and the curves differ slightly between the materials. Cycling the final three times (as in figure 4(b)) gave closely overlapping curves that are different in shape with a lower 0% strain slope B of 710 kPa than the initial extension curve 1 with slope A of 790 kPa for the CF18-2186 control. Similar Mullins effect behavior was observed for the 225-1. At first glance, the longitudinal printed membranes have a similar maximum elongation at break and UTS to the controls for both materials. Specifically, for CF18-2186 the failure points were 370% and 2.05 MPa for the longitudinal printed film and 355% and 1.54 MPa for the blade-cast control. Similarly, for 225-1 the failure points were 405% and 1.39 MPa for the longitudinal printed film and 485% and 1.97 MPa for the control. In addition, for both materials the transverse printed group appears to have a higher maximum elongation and UTS than the longitudinal and control groups.

Table 2. Various properties of the printed thermal and UV-cure silicone membranes in figure 3. All membranes were printed on-the-fly at 50 mm s^{-1}.

Figures	Printed material	Average thickness (μm)	Thickness standard deviation σ (μm)	Jetting frequency (Hz)	Number of drops jetted	Drop spacing (μm)	Printed resolution (dpi/dpc)
3(a)	Wacker Elastosil® P7670	4.1	0.22	330	33^2 (1089)	151.5	168/66
3(b)	NuSil CF18-2186	4.0	0.28	450	45^2 (2025)	111.1	229/90
3(c)	Bluestar Silbione® LSR 4305	3.7	0.73	500	50^2 (2500)	100.0	254/100
3(d)	Wacker Silpuran® 6000/05	2.0	0.20	300	30^2 (900)	166.7	152/60
3(e)	Momentive Electro 225-1	2.3	0.06	480	48^2 (2304)	104.2	244/96
3(f)	NuSil CF18-2186	4.5	0.42	450	90^2 (8100)	111.1	229/90

Table 3. Averaged tensile mechanical properties of the silicone membranes presented in figure 5. Data are given as mean ± standard error, and the number of samples that were averaged is given as *N*.

Material	Group	Ultimate tensile strength (MPa)	Maximum elongation (%)	Young's modulus (kPa)
NuSil CF18-2186	Cast control	1.67 ± 0.57 ($N = 5$)	330 ± 77 ($N = 5$)	710 ± 26 ($N = 3$)
	Transverse printed	1.96 ± 0.51 ($N = 3$)	377 ± 62 ($N = 3$)	686 ± 27 ($N = 3$)
	Longitudinal printed	1.38 ± 0.28 ($N = 4$)	285 ± 39 ($N = 4$)	712 ± 16 ($N = 4$)
Momentive UV Electro 225-1	Cast control	1.55 ± 0.15 ($N = 6$)	395 ± 27 ($N = 6$)	655 ± 33 ($N = 6$)
	Transverse printed	3.19 ± 0.82 ($N = 3$)	603 ± 63 ($N = 3$)	760 ± 40 ($N = 3$)
	Longitudinal printed	0.94 ± 0.44 ($N = 2$)	277 ± 128 ($N = 2$)	677 ± 62 ($N = 2$)

The transverse failure points were 462% and 2.5 MPa for CF18-2186 and 727% and 4.84 MPa for 225-1. More concrete conclusions on the mechanical performance are drawn from statistical analysis below in figure 5, in which the means and standard errors of several sample trials are compared rather than single trials as in figure 4.

Figure 4(d) is a photograph of one such 225-1 membrane under test at 600% strain right before the moment of failure. Under reflected light, it was highly colored due to thin film interference, in which the color is a function of the film thickness. The instantaneous colors can therefore be a qualitative measure of the film homogeneity. In the photograph, the primary hue is a purple-red with light banding visible, although the color and hence thickness is fairly homogenous in the center region. The edges show a variety of colors from reds to blues, indicating different instantaneous thicknesses that are greater than the center thickness due to the catenary structures present. In addition, since the film thickness changed during the pull test, the color also changed. Hence film color changes could be used a metric of the film thickness changes. Changes in the thin film interference colors were also observed during prestretching of printed and blade-cast silicone circles prior to actuation, whose actuation results are shown in the next section.

Statistical analysis was performed on the physical properties of UTS, maximum elongation, and Young's modulus for both materials in order to compare the printed samples to the cast control samples. The results are given in table 3 and plotted in figure 5. Unless stated otherwise, statistical data reported with an error but with no standard deviation (σ) has the format: mean ± standard error, in which standard error $= \sigma/\sqrt{N}$. This allows for easy comparison of the means. The sample size (N) is also given so the standard deviation can be calculated for each mean.

As seen in the first row of figure 5, the standard error bars overlap, meaning that for all CF18-2186 properties, there is no statistically significant difference among mean groups. Hence for CF18-2186, printing in either orientation gives the same mechanical properties as blade casting the material. Similarly, there is no statistically significant difference among groups for the 225-1 tensile strength. Although the standard error bars do not overlap for the 225-1 Young's modulus cast control and transverse printed groups, the difference is not statistically significant, as determined by an unpaired t test with a two-tailed P value of 0.101. Thus the 225-1 Young's modulus and tensile strength are the same for printing in either orientation as for blade casting. However, for the 225-1 elongation at break the difference is very statistically significant between the means of the cast control and transverse printed groups ($P = 0.0080$), but the difference between the means of the longitudinal and transverse printed groups is almost statistically significant ($P = 0.0801$), likely since the sample size N is smaller. As the error bars overlap, there is no statistically significant difference between the longitudinal printed and cast control for the 225-1 elongation at break ($P = 0.1818$). This may imply that printing the 225-1 in the transverse direction confers some advantage to the maximum elongation, but further experimentation is needed to draw this conclusion with certainty. In summary, it can at least be concluded that printing either the thermal cure CF18-2186 or the UV cure 225-1, with a raster in either direction, produces silicone films with mechanical properties that are as good as films prepared from the standard blade casting preparation technique. This is especially interesting for the CF18 because parts A and B were printed separately before curing, whereas parts A and B were mixed prior to blade casting and curing.

In almost all samples, the Mullins effect was apparent, in which curve 1 had a higher initial slope than curves 3, 5, and 7 (as in figure 4(b), which shows only one CF18-2186 control sample). The average initial 0% strain slopes for NuSil CF18-2186 blade-cast control, transverse printed, and longitudinal printed were: 1150 ± 256 kPa ($N = 3$), 1180 ± 130 kPa ($N = 3$), and 1190 ± 186 kPa ($N = 4$), respectively. Similarly, the average initial 0% strain slopes for Momentive UV Electro 225-1 blade-cast control, transverse printed, and longitudinal printed were: 854 ± 160 kPa ($N = 6$), 943 ± 114 kPa ($N = 3$), and 533 ± 142 kPa ($N = 2$), respectively. In all cases except the final mean, the initial slope was always higher than the Young's modulus slopes taken from curves 3%, 5% and 7 at 0% strain. However, by an unpaired t test, the slope difference between curve 1 and curve 3 is statistically significant for only CF18-2186 transverse ($P = 0.0205$) and longitudinal printed ($P = 0.0429$). The difference is not statistically significant for: CF18-2186 control ($P = 0.1624$),

225-1 control ($P = 0.2511$), 225-1 transverse ($P = 0.2044$), and 225-1 longitudinal ($P = 0.4508$). From the given data, this may imply that the Mullins effect is less pronounced for the 225-1 than for the CF18-2186, although in general the initial curve 1 slope was higher than the slope of curves 3, 5, or 7. And in the case of 225-1 longitudinal, the mean slope of curve 3 is smaller than that of curve 1, but the standard errors overlap and the difference is not significant.

4.3. DEA electromechanical performance

The performance of printed NuSil CF18-2186 and Momentive 225-1 silicone films as dielectric membranes in DEAs was investigated. We find that DEAs made using the printed thermal-cure CF18-2186 and the UV-cure 225-1 silicone films have actuation properties that are as good as DEAs made with films of comparable thickness prepared using the standard blade casting technique. A completed miniature DEA is shown in the inset in figure 6(a). Actuation performance of blade-cast membranes of the same material were also investigated for comparison. These blade-cast control samples were pad-printed and prestreched using the same procedure as that applied to the inkjet printed silicone samples.

In figure 6(a), the actuation performance for DEAs made with NuSil CF18-2186 is presented for one cast (red curve, 3.4 μm dielectric thickness) and one printed (black curve, 11.0 μm thick dielectric) membrane. The maximum area strains for both are comparable, although the printed membrane shows a slightly higher maximum diametral actuation strain and breakdown field. The printed CF18-2186 had a maximum strain of 6.1% at a nominal electric field of 84.0 V μm^{-1}, while the blade-cast control actuator had a maximum strain of 3.9% at a field of 82.4 V μm^{-1} nominal. Shown in figure 6(b) is the area strain versus nominal electric field of three different DEAs with inkjet printed dielectrics of Momentive 225-1, as well as one blade-cast control sample (red curve, 3.4 μm dielectric thickness). The printed devices show a slight distribution of characteristics. These ranged from 4.7% maximum area strain at 99 V μm^{-1} (the black curve, for a 3.3 μm dielectric thickness), to 2.5% strain at 116.2 V μm^{-1} (blue curve, 2.7 μm thick dielectric), and finally to 2.4% strain at 129.6 V μm^{-1} (green curve, 3.2 μm dielectric). Globally the printed DEAs achieved roughly the same maximum area strain as that of the control.

Some variability in strain is expected for DEAs with thin (<4 μm) dielectrics where the pad printing process could result in electrodes of varying thickness and stiffness and where the membrane thickness and prestretch could show small variations. Future work involving printing an entire DEA, including the electrodes, may result in more consistent actuation results. In short, both the printed thermal-cure CF18-2186 and the UV-cure 225-1 silicone films have actuation properties that are as good as films prepared from the standard blade casting technique. There is no apparent alteration in dielectric film quality as a result of the inkjet printing process reported in this work.

5. Conclusion and outlook

Additive manufacturing, and most notably 3D printing, of dielectric elastomer devices can offer many advantages over traditional DEA fabrication techniques. In general, 3D printing offers many manufacturing benefits as a result of computer control, such as full automation, high resolution, potentially consistent results, predictable production yields, relatively low production costs, and flexible designs that are fully defined from a CAD file. 3D printing can also fabricate unique, potentially complex features that are made from multiple different materials and can be fully integrated with no further assembly required. In addition to all of these many strengths, 3D printing is of interest to manufacturing DEA-based devices also because it can print very thin dielectric elastomer layers of 2 μm or less, resulting in lower driving voltages. Of the many types of 3D printing technologies, piezoelectric DOD inkjet systems offer today the best combination of high resolution, low cost, and breadth of printable materials for DEAs. The ability to print commercially available true rubber materials is critical to producing highly reliable, high-performance DEA devices, rather than printing pseudo-rubbers that often lack the required electromechanical integrity.

In our novel approach, commercially available DEA silicone materials have been successfully 3D printed with a DOD, piezoelectric inkjet system. With proper ink formulation and waveform design, stable, satellite-free drops can be formed from inks prepared from dilutions of these silicone rubbers. Inks with lower pre-dilution pot viscosities result in the best quality silicone films. With this DOD approach, drop spacing can be tuned to produce optimal film quality. UV or thermal curing is fast and can be performed *in situ*. UV-cure silicones can be printed and cured on-the-fly in seconds. Likewise, each component ink of thermal cure silicones can be printed separately, one on top of the other, and then cured in seconds via thermal conduction or IR spot curing. Printing complex 3D structures of silicone elastomer is possible, as demonstrated by 3D printing the high-resolution, two-level EPFL logo from a UV-curable silicone rubber. Importantly, the mechanical properties and actuation performance of the 3D printed DEA silicone membranes were at least as good as those of blade-cast control silicone membranes. Therefore, the manufacturing technique presented in this paper of inkjet printing high-quality silicone elastomer membranes for DEAs is a viable alternative to more traditional manufacturing techniques. This holds great promise for the future of the DEA field, which is moving toward producing more complex integrated DEA devices by utilizing automation through high-precision computer control.

Acknowledgments

We gratefully acknowledge members of the EPFL-LMTS for hopeful comments and discussion. This work was partially funded by the European Union's Horizon 2020 research and innovation programme under the Marie Skłodowska-Curie

grant agreement No. 641822—MICACT via the Swiss State Secretariat for Education, Research, and Innovation.

ORCID iDs

Herbert Shea https://orcid.org/0000-0003-3527-3036

References

[1] Pelrine R, Kornbluh R, Joseph J, Heydt R, Pei Q and Chiba S 2000 High-field deformation of elastomeric dielectrics for actuators *Mater. Sci. Eng.* C **11** 89–100

[2] Brochu P and Pei Q 2010 Advances in dielectric elastomers for actuators and artificial muscles *Macromol. Rapid Commun.* **31** 10–36

[3] Anderson I A, Gisby T A, McKay T G, O'Brien B M and Calius E P 2012 Multi-functional dielectric elastomer artificial muscles for soft and smart machines *J. Appl. Phys.* **112** 041101

[4] Rosset S and Shea H R 2016 Small, fast, and tough: Shrinking down integrated elastomer transducers *Appl. Phys. Rev.* **3** 031105

[5] Rosset S, Araromi O A, Schlatter S and Shea H R 2016 Fabrication process of silicone-based dielectric elastomer actuators *J. Vis. Exp.* **108** 53423

[6] Rosset S and Shea H R 2013 Flexible and stretchable electrodes for dielectric elastomer actuators *Appl. Phys.* A **110** 281–307

[7] McCoul D, Hu W, Gao M, Mehta V and Pei Q 2016 Recent advances in stretchable and transparent electronic materials *Adv. Electron. Mater.* **2** 1500407

[8] Murray C, McCoul D, Sollier E, Ruggiero T, Niu X, Pei Q and Di Carlo D 2013 Electro-adaptive microfluidics for active tuning of channel geometry using polymer actuators *Microfluidics Nanofluidics* **14** 345–58

[9] Maffli L, Rosset S and Shea H 2013 Zipping dielectric elastomer actuators: characterization, design and modeling *Smart Mater. Struct.* **22** 104013

[10] Price A K and Culbertson C T 2009 Generation of nonbiased hydrodynamic injections on microfluidic devices using integrated dielectric elastomer actuators *Anal. Chem.* **81** 8942–8

[11] Poulin A, Saygili Demir C, Rosset S, Petrova T V and Shea H 2016 Dielectric elastomer actuator for mechanical loading of 2D cell cultures *Lab Chip* **16** 3788–94

[12] Akbari S and Shea H 2012 Microfabrication and characterization of an array of dielectric elastomer actuators generating uniaxial strain to stretch individual cells *J. Micromech. Microeng.* **22** 045020

[13] Maffli L, Rosset S, Ghilardi M, Carpi F and Shea H 2015 Ultrafast all-polymer electrically tunable silicone lenses *Adv. Funct. Mater.* **25** 1656–65

[14] Romano P, Araromi O, Rosset S, Shea H and Perruisseau-Carrier J 2014 Tunable millimeter-wave phase shifter based on dielectric elastomer actuation *Appl. Phys. Lett.* **104** 024104

[15] Niu X, Brochu P, Stoyanov H, Yun S R and Pei Q 2012 Bistable electroactive polymer for refreshable Braille display with improved actuation stability *Proc. SPIE* **8340** 83400R

[16] Ren Z, Niu X, Chen D, Hu W and Pei Q 2014 A new bistable electroactive polymer for prolonged cycle lifetime of refreshable Braille displays *Proc. SPIE* **9056** 905621

[17] Carpi F, Frediani G and De Rossi D 2009 Electroactive elastomeric haptic displays of organ motility and tissue compliance for medical training and surgical force feedback *IEEE Trans. Biomed. Eng.* **56** 2327–30

[18] Carpi F, Mannini A and De Rossi D 2009 Dynamic splint-like hand orthosis for finger rehabilitation *Biomedical Applications of Electroactive Polymer Actuators* (New York: Wiley) p 443–61

[19] Kovacs G, Lochmatter P and Wissler M 2007 An arm wrestling robot driven by dielectric elastomer actuators *Smart Mater. Struct.* **16** S306

[20] Biddiss E and Chau T 2008 Dielectric elastomers as actuators for upper limb prosthetics: challenges and opportunities *Med. Eng. Phys.* **30** 16

[21] Carpi F, Migliore A, Serra G and De Rossi D 2005 Helical dielectric elastomer actuators *Smart Mater. Struct.* **14** 1210–6

[22] Carpi F, Salaris C and De Rossi D 2007 Folded dielectric elastomer actuators *Smart Mater. Struct.* **16** S300

[23] Shintake J, Rosset S, Schubert B, Floreano D and Shea H 2016 Versatile soft grippers with intrinsic electroadhesion based on multifunctional polymer actuators *Adv. Mater.* **28** 231–8

[24] Graf N J and Bowser M T 2008 A soft-polymer piezoelectric bimorph cantilever-actuated peristaltic micropump *Lab Chip* **8** 1664–70

[25] Pan T, McDonald S J, Kai E M and Ziaie B 2005 A magnetically driven PDMS micropump with ball check-valves *J. Micromech. Microeng.* **15** 1021

[26] McCoul D, Samuel R, Nadine B and Herbert S 2017 Multifunctional shape memory electrodes for dielectric elastomer actuators enabling high holding force and low-voltage multisegment addressing *Smart Mater. Struct.* **26** 025015

[27] Jung K, Koo J C, Lee Y K and Choi H R 2007 Artificial annelid robot driven by soft actuators *Bioinsp. Biomim.* **2** S42

[28] Jordi C, Michel S and Fink E 2010 Fish-like propulsion of an airship with planar membrane dielectric elastomer actuators *Bioinsp. Biomim.* **5** 026007

[29] Pelrine R, Kornbluh R, Joseph J and Chiba S 1997 Electrostriction of polymer films for microactuators *Proc. IEEE The 10th Annual Int. Workshop on Micro Electro Mechanical Systems. An Investigation of Micro Structures, Sensors, Actuators, Machines and Robots* (https://doi.org/10.1109/MEMSYS.1997.581811)

[30] Schlaak H F, Jungmann M, Matysek M and Lotz P 2005 Novel multilayer electrostatic solid state actuators with elastic dielectric *Smart Structures and Materials 2005: Electroactive Polymer Actuators and Devices (EAPAD)* vol 5759, p 13

[31] Maas J, Tepel D and Hoffstadt T 2015 Actuator design and automated manufacturing process for DEAP-based multilayer stack-actuators *Meccanica* **50** 2839–54

[32] Vaezi M, Seitz H and Yang S 2013 A review on 3D micro-additive manufacturing technologies *Int. J. Adv. Manuf. Technol.* **67** 1721–54

[33] Kruth J P, Leu M C and Nakagawa T 1998 Progress in additive manufacturing and rapid prototyping *CIRP Ann.—Manuf. Technol.* **47** 525–40

[34] Zolfagharian A, Kouzani A Z, Khoo S Y, Moghadam A A A, Gibson I and Kaynak A 2016 Evolution of 3D printed soft actuators *Sensors Actuators* A **250** 258–72

[35] Truby R L and Lewis J A 2016 Printing soft matter in three dimensions *Nature* **540** 371–8

[36] Lee B H, Abdullah J and Khan Z A 2005 Optimization of rapid prototyping parameters for production of flexible ABS object *J. Mater. Process. Technol.* **169** 54–61

[37] Sood A K, Ohdar R K and Mahapatra S S 2009 Improving dimensional accuracy of fused deposition modelling processed part using grey taguchi method *Mater. Des.* **30** 4243–52

[38] Anitha R, Arunachalam S and Radhakrishnan P 2001 Critical parameters influencing the quality of prototypes in fused deposition modelling *J. Mater. Process. Technol.* **118** 385–8
[39] Shirazi S F S, Gharehkhani S, Mehrali M, Yarmand H, Metselaar H S C, Kadri N A and Osman N A A 2015 A review on powder-based additive manufacturing for tissue engineering: selective laser sintering and inkjet 3D printing *Sci. Technol. Adv. Mater.* **16** 033502
[40] Gross B C, Erkal J L, Lockwood S Y, Chen C and Spence D M 2014 Evaluation of 3D printing and its potential impact on biotechnology and the chemical sciences *Anal. Chem.* **86** 3240–53
[41] Melchels F P W, Feijen J and Grijpma D W 2010 A review on stereolithography and its applications in biomedical engineering *Biomaterials* **31** 6121–30
[42] Choi J-W, Kim H-C and Wicker R 2011 Multi-material stereolithography *J. Mater. Process. Technol.* **211** 318–28
[43] Kumpulainen T, Pekkanen J, Valkama J, Laakso J, Tuokko R and Mäntysalo M 2011 Low temperature nanoparticle sintering with continuous wave and pulse lasers *Opt. Laser Technol.* **43** 570–6
[44] Bertol L S, Júnior W K, Silva F P D and Aumund-Kopp C 2010 Medical design: direct metal laser sintering of Ti–6Al–4V *Mater. Des.* **31** 3982–8
[45] Simchi A and Pohl H 2003 Effects of laser sintering processing parameters on the microstructure and densification of iron powder *Mater. Sci. Eng.* A **359** 119–28
[46] Kumar S 2003 Selective laser sintering: a qualitative and objective approach *JOM* **55** 43–7
[47] Derby B 2010 Inkjet printing of functional and structural materials: fluid property requirements, feature stability, and resolution *Annu. Rev. Mater. Res.* **40** 395–414
[48] Khoo Z X, Teoh J E M, Liu Y, Chua C K, Yang S, An J, Leong K F and Yeong W Y 2015 3D printing of smart materials: a review on recent progresses in 4D printing *Virtual Phys. Prototyping* **10** 103–22
[49] Araromi O A, Conn A T, Ling C S, Rossiter J M, Vaidyanathan R and Burgess S C 2011 Spray deposited multilayered dielectric elastomer actuators *Sensors Actuators* A **167** 459–67
[50] Reitelshöfer S, Landgraf M, Graf D, Bugert L and Franke J 2015 A new production process for soft actuators and sensors based on dielectric elastomers intended for safe human robot interaction *IEEE/SICE Int. Symp. on System Integration (SII)* pp 51–6
[51] Reitelshöfer S, Göttler M, Schmidt P, Treffer P, Landgraf M and Franke J 2016 Aerosol-jet-printing silicone layers and electrodes for stacked dielectric elastomer actuators in one processing device *Proc. SPIE* **9798** 97981Y
[52] Poulin A, Rosset S and Shea H R 2015 Printing low-voltage dielectric elastomer actuators *Appl. Phys. Lett.* **107** 244104
[53] Rossiter J, Walters P and Stoimenov B 2009 Printing 3D dielectric elastomer actuators for soft robotics *Proc. SPIE* (https://doi.org/10.1117/12.815746)
[54] Baechler C, Gardin S, Abuhimd H and Kovacs G 2016 Inkjet printed multiwall carbon nanotube electrodes for dielectric elastomer actuators *Smart Mater. Struct.* **25** 055009
[55] Schlatter S, Rosset S and Shea H R 2017 Inkjet printing of carbon black electrodes for dielectric elastomer actuators *Proc. SPIE* **10163** 1016311
[56] Kurian A S, Giffney T, Lee J, Travas-Sejdic J and Aw K C 2016 Printing of CNT/silicone rubber for a wearable flexible stretch sensor *Proc. SPIE* **9798** 97980K
[57] Tekin E, Smith P J and Schubert U S 2008 Inkjet printing as a deposition and patterning tool for polymers and inorganic particles *Soft Matter* **4** 703–13
[58] de Gans B J, Duineveld P C and Schubert U S 2004 Inkjet printing of polymers: state of the art and future developments *Adv. Mater.* **16** 203–13
[59] A-Alamry K, Nixon K, Hindley R, Odel J A and Yeates S G 2011 Flow-induced polymer degradation during ink-jet printing *Macromol. Rapid Commun.* **32** 316–20
[60] McKinley G H 2005 Dimensionless groups for understanding free surface flows of complex fluids *Soc. Rheol. Bull.* **2005** 6–9
[61] McKinley G H 2005 Visco-elasto-capillary thinning and break-up of complex fluids *Annu. Rheol. Rev.* **2005** 1–48
[62] Morrison N F and Harlen O G 2010 Viscoelasticity in inkjet printing *Rheol. Acta* **49** 619–32
[63] Mullins L 1969 Softening of rubber by deformation *Rubber Chem. Technol.* **42** 339–62
[64] Project Peta-pico-Voltron: High Voltage Power Supply 2017 http://petapicovoltron.com (17 August 2017)
[65] Deegan R D, Bakajin O, Dupont T F, Huber G, Nagel S R and Witten T A 1997 Capillary flow as the cause of ring stains from dried liquid drops *Nature* **389** 827–9